Int. J. Heat Mass Transfer. Vol. 36, No. 9, pp. 2457–2471, 1993
Printed in Great Britain

0017-9310/93 $6.00 + 0.00

An experimental study of laminar entrance flow and heat transfer in finned tube annuli

SHOU-SHING HSIEH† and CHANG-CHUN LIN
Department of Mechanical Engineering, National Sun Yat-Sen University, Kaohsiung, Taiwan 80424, R.O.C.

(*Received* 16 *July* 1991 *and in final form* 10 *December* 1991)

Abstract—In this study, experiments were conducted to investigate the entrance effect of a double-pipe heat exchanger with isoflux inner finned tube. The geomery of the test section varied in fin pitch to height (p/e) ratios from 4 to 12, in fin width to height ratios (w/e) of 0.14 and 0.83, and with two inner diameter to outer diameter ratios (D_i/D_o) of 0.38–0.51. Reynolds numbers (Re) of the flow were 100–3000. To gather detailed information regarding the flow and heat transfer measurements, flow visualization as well as qualitative information of thermal fields using holographic techniques were made and analyzed. Results are presented for a range of Reynolds number and for various values of the geometrical parameters. The experimental data were extracted and correlated in the form of Graetz number (Gz) to provide a thermal design basis for engineering application.

1. INTRODUCTION

HEAT TRANSFER from rough surfaces has received a great deal of attention [1–3] due to the many practical applications for increasing the effectiveness of heat transfer and the difficulty in obtaining analytical solutions for the temperature and velocity fields. Laminar flow heat transfer occurs in a variety of engineering problems and is of particular importance where viscous liquids are heated or cooled. Since the heat transfer coefficients in this type of flow are generally low, there is a need for augmentation. Moreover, the length of the test section in the previous studies was long enough to guarantee that the flow was fully developed. However, in many practical applications, due to the cost of material and space limitations, the length of the tube is shorter than that used in previous studies. Since the smooth tube performs rather poorly under laminar conditions, the need for heat transfer augmentation is actually greater in laminar tube flow. In addition, many flows are laminar because of small dimensions, low flow rates or highly viscous fluids. Accordingly, roughened configurations are needed to enhance the rate of heat transfer.

Most flow problems in industrial heat exchangers involve turbulent flow. Attention has been directed mainly towards turbulent flow heat transfer augmentation, and only a very limited amount of literature is available on laminar flow heat transfer enhancement [4–6]. A review of the published results in the field was recently reported by Bergles and Joshi [7].

Measurements of heat transfer and pressure drop in a parallel plate channel with triangular corrugations were done by O'Brien and Sparrow [8]. The heat transfer was found to increase by a factor of 2.5 with an increase in the pressure drop by an order of magnitude. This is because of the high friction factor of about 0.57. Webb and Ramadhyani [9] studied laminar flow and heat transfer in a similar passage with straight fins. It was found that fins with an aspect ratio of 6, which caused a reduction of 25% in flow rate, provided the best compromise between increases in the heat transfer and the pressure drop. Under such a condition, heat transfer augmentation could be justified only for high Prandtl number ($\geqslant 7$) fluids. A similar study done by Kelkar and Patankar [10] with conducting fins was 30–50% more efficient due to non-conducting fins. At low Prandtl numbers, the fins actually reduced the heat transfer.

Flow and heat transfer in a tube with internal circumferential fins of height comparable to the tube diameter were studied by Rowley and Patankar [11]. Despite the increased surface area provided by the fins, the heat transfer could decrease due to the flow diversion. This is so because recirculating flow in the wake of the fins increases mixing, but the fins cause the main flow to move away from the heated wall. Consequently, the total heat transfer decreases except at high Prandtl numbers.

Laminar flow and heat transfer in an annulus with a wavy inner tube were studied by Prata and Sparrow [12] and Agrawal and Sengupta [13]. Wavy inner tubes were found to be attractive since they provided heat transfer enhancement with a small increase in the pressure drop. In view of the foregoing discussion, the present study is limited to the entrance region, and the flow is laminar and steady. Enhancement by external circular conducting fins and entrance effects are investigated. A finned tube with uniform heat flux is placed inside a circular tube. Pressure drop and heat transfer characteristics are obtained with varied fin height and

† Author to whom correspondence should be addressed.

NOMENCLATURE

A_s	heat transfer area, $2\pi r_c L$ [m]
D_h	hydraulic diameter, $2(R_o - R_i)$ [mm]
e	fin height [mm]
f_{app}	friction factor, $\Delta p^* D_h/x$
Gz	Graetz number, $Re\,Pr\,(D_h/x)$
h_x	local heat transfer coefficient, $q''/(T_w - T_m)$ [W m^{-1} K^{-1}]
Nu_x	local Nusselt number, $h_x D_h/K_f$
p	fin spacing [mm]
Δp^*	dimensionless pressure drop, $2\Delta P/(\rho W_m^2)$
ΔP	pressure drop [kg s^{-2} m^{-1}]
q''	heat flux [W m^{-2}]
r_c	radius of equivalence circular tube defined in equation (4) [mm]
Re	Reynolds number based upon D_h, $W_m D_h/v$
T_f	reference fluid temperature, defined in equation (1) [°C]
T_m	bulk temperature, $\int_{r_i}^{r_o} T(r) W_m(r) r\,dr / (\int_{r_i}^{r_o} W_m(r) r\,dr)$ [°C]
T_w	inlet inner wall temperature
w	fin width [mm]
W_m	mean axial velocity used in equation (2) [m s^{-1}]
x	axial distance [mm]
x^+	dimensionless axial distance, $x/(D_h\,Re)$.

Greek symbols

v	kinematic viscosity [m^2 s^{-1}]
ρ	density [kg m^{-3}].

Subscripts

1	inlet
2	outlet
al	alcohol
i	inner wall
o	outer wall.

pitch. Effects of the Reynolds number and the physical geometry for enhancement in thermal developing flow are presented and discussed.

2. EXPERIMENTAL APPARATUS AND PROCEDURE

The experimental apparatus is made of a conventional double-pipe heat exchanger. Figures 1(a) and (b) show a schematic drawing of the experimental apparatus. The inside diameter of the outer tube (D_o) is 130 mm with the outside diameter (D_i) of the isoflux a heated inner tube of 52 mm. The outer surface of the inner tube was roughened by using annular steel fins of high thermal conductivity ($K = 54$ W m^{-1} °C^{-1}).

Four pitch-to-height ratios of $p/e = 4$, 6, 9 and 12, with two width-to-height ratios of $w/e = 0.14$ and 0.83 were tested in the present study. Detailed data are given in Table 1. Twenty-one pairs of Chromel–Alumel (28 AWG) thermocouples were used to measure the temperature distribution of the inner tube between tube fins for $w/e = 0.14$ and Fig. 1(c) shows details of the thermocouple placement. The tem-

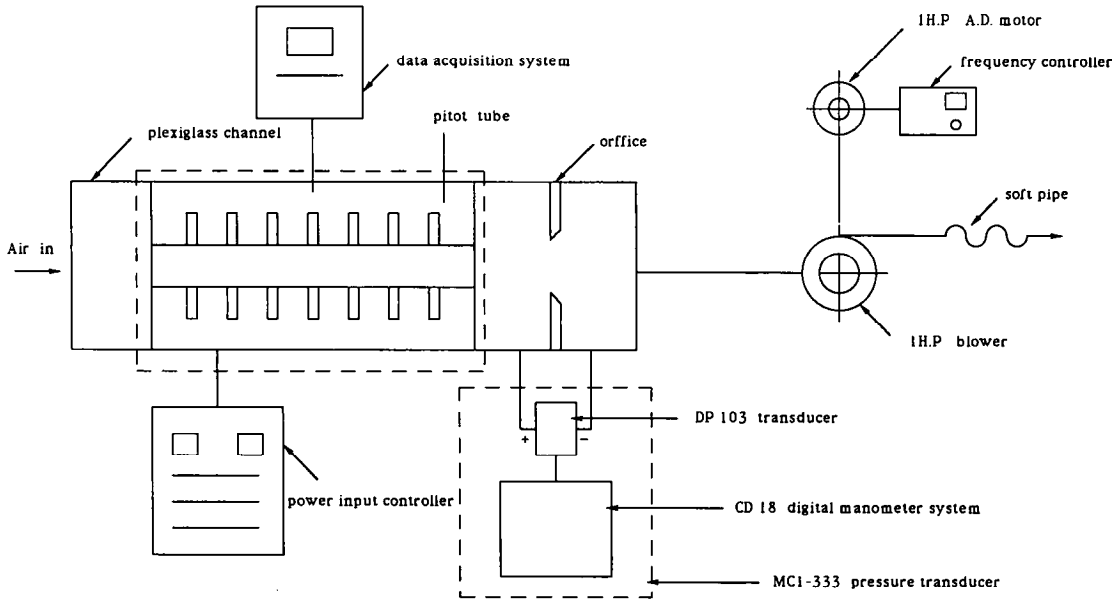

FIG. 1(a). Schematic of experimental apparatus.

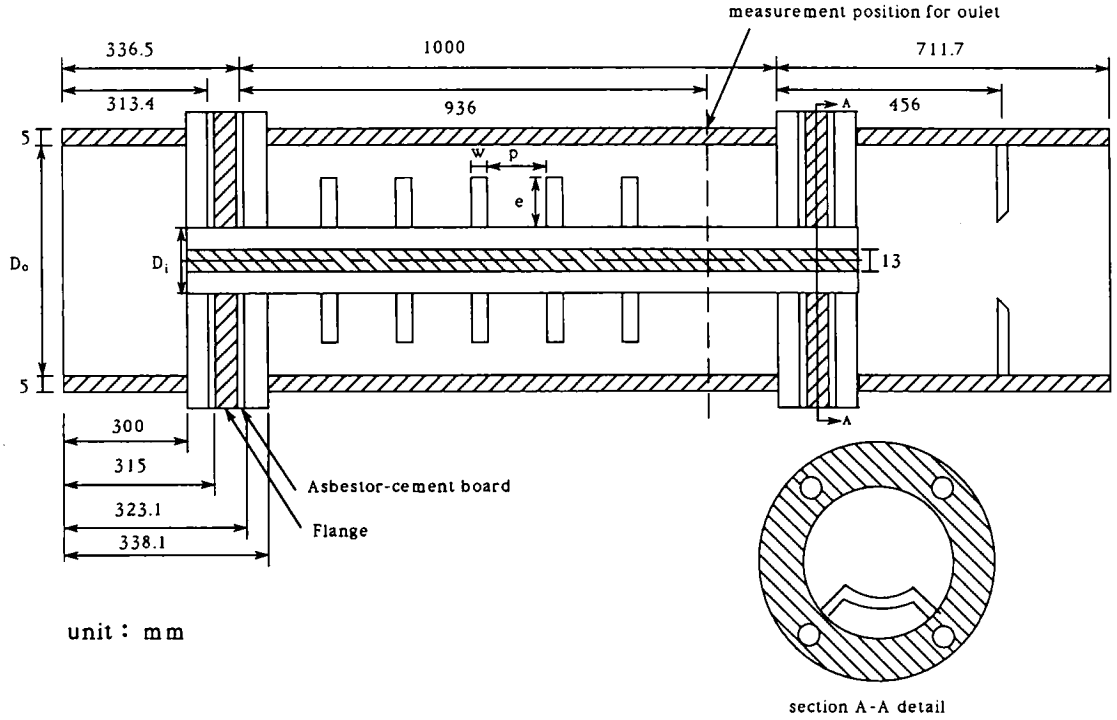

FIG. 1(b). Detailed structure for test pipe.

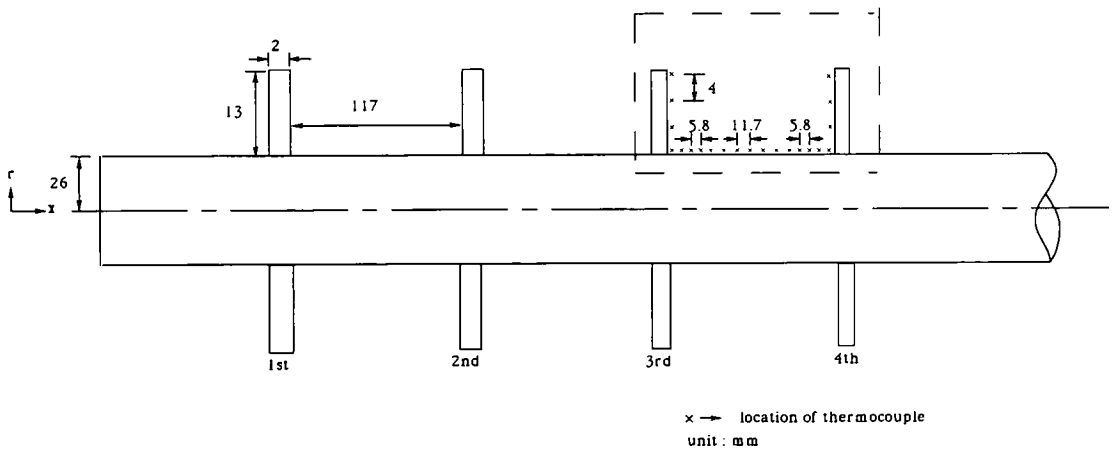

FIG. 1(c). Temperature measurement position.

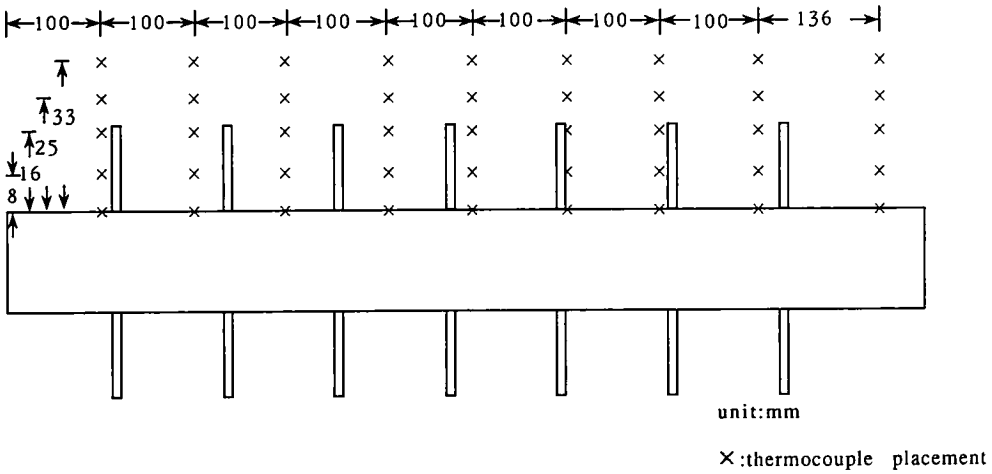

FIG. 1(d). Thermocouple placement for typical local mean axial temperature measurement ($p/e = 6$).

Table 1. Detailed size for inner test annuli

Test annulus	p (mm)	e (mm)	D_h (mm)	Number of fin elements	A_s (m^2)	p/e
Fin	78	19.5	42.97	11	0.2734	4
Fin	117	19.5	55.31	7	0.2346	6
Fin	117	13.0	64.70	7	0.2051	9
Fin	156	13.0	68.53	5	0.1931	12
Smooth			54.00		0.2388	

perature measurement points shown in Fig. 1(d) are located at $x = 100$, 200, 300, 400, 500, 600, 700, 800 and 936 mm.

The thermocouples were connected to an HP-3054DL data acquisition system. By means of HP-85B PC software, the measured voltage is converted into temperature automatically and with an accuracy of ± 0.7°C.

The data presented are for air ($Pr \approx 0.7$) with an approximate power input of $Q = 68.54$ W for each test inner tube. The inner tube consists of two parts: one is the hollow circular pipe of SS41 steel 2 mm thick, the other is the heater covered with a stainless steel pipe with a diameter of 13 mm. A heat sink compound (MgO) was filled between the heater and the stainless steel circular pipe to reduce contact resistance. The detailed structure is shown in Fig. 2. Stationary water was chosen to fill the space between heater and steel tube because of its stable property in the range of temperature 48–82°C for test tubes. Thermocouples as well as pitot tubes were also placed at different radial portions (five points for each measurement for velocity distribution curve fitting) in the inlet and outlet of the test section to estimate the bulk temperature (see Fig. 1(d) for details). In addition, thermocouples were placed at different positions along the inside of the outer tube to estimate the conduction loss. The conduction losses through the wall of the outer tube were also calculated to obtain the net energy transported by convective fluid. In general, the conduction loss is within 3.75% of the total input for the present experiments.

In addition to temperature measurement at the inlet and outlet, two pressure ports in the pitot tube are connected to DP-103 transducers. By means of a CD-18 digital manometer system, the measured pressure is converted into voltage automatically, and converted into readings in velocity at different radial positions

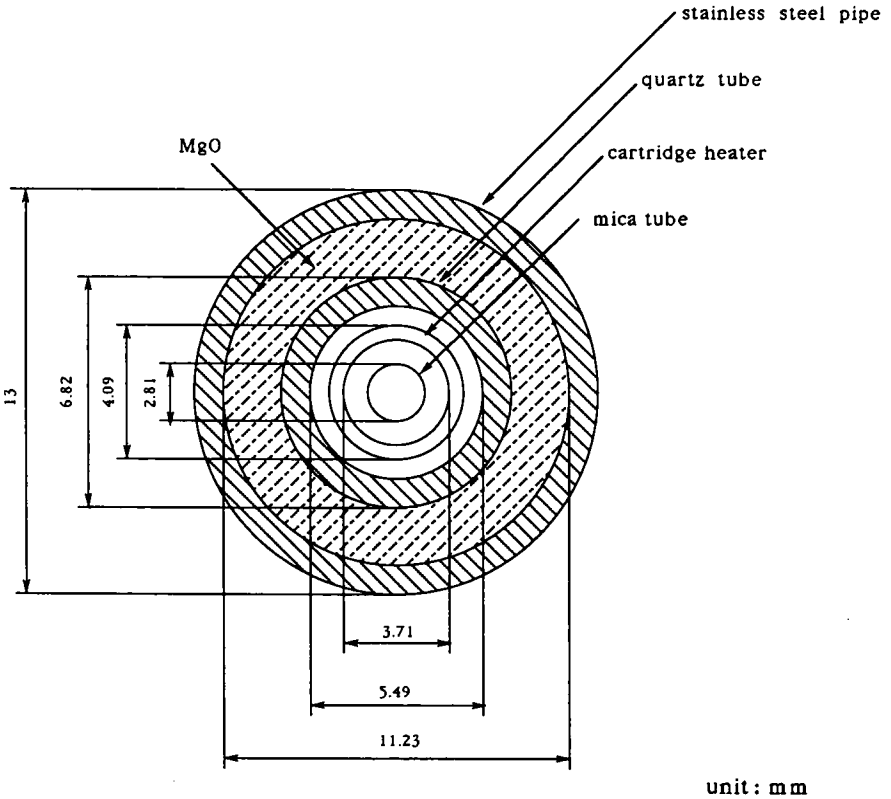

FIG. 2. Details of heating element.

at the inlet and outlet. The total flow is measured by an orifice plate placed downstream of the test section. The pressure distribution along the outer wall is obtained by an MC1-333 pressure transducer with an accuracy up to ± 0.01 cm of water. Pressure at the inlet is specified as zero.

To examine the flow structure, flow visualization experiments were conducted for several Reynolds numbers. The smoke generation method was applied with straw smoke and air as the convection medium to visualize the flow. The illumination of the smoke was done by using a slide projector as a light source. When the condition was steady, the smoke was supplied through a plexiglass pipe to a plastic rake located in the wind tunnel. All photographs were taken with a Cannon-T70 camera on Konica HR 1600 films with exposure times of 1/30–1/60 s. Furthermore, the test tubes were placed in the test beam of a laser holographic interferometer for further study of the thermal characteristics. The laser holographic interferometry used in this study is essentially the same as that described by Aung and O'Regan [14] and is shown schematically in Fig. 3. Coherent light (0.638 μm) from a 35 mW Spectra-Physics model 124-B He–Ne laser is split into an object beam and a reference beam by a variable silvered mirror, and each beam is expanded to a 90 mm planar wave via a $\times 20$ microscopic objective, a $\times 60$ microscopic objective, and two collimating lenses (diameter 12.7 cm). Pinholes of 20 μm diameter are located at the focal points of the microscopic objectives in order to eliminate intensity variations in the wave fronts. The two wave fronts intersect at the photographic plate (here at an angle of 20°) and produce a hologram when the photographic emulsion is exposed simultaneously to the two beams and then developed *in situ*. The interferometer components and test section are mounted securely on a 1.4×2.0 m vibration-free optical table.

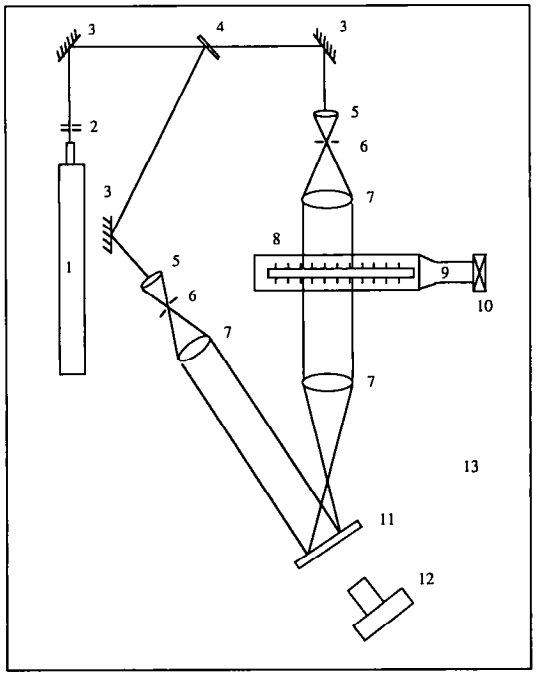

FIG. 3. Schematic of holographic interferometer for thermal field: 1, helium–neon laser; 2, shutter; 3, mirror; 4, beam splitter; 5, objective lens; 6, pinhole; 7, collimating lens; 8, test section; 9, duct; 10, blower; 11, holographic plate; 12, camera; 13, vibration-free optical table.

3. UNCERTAINTY ANALYSIS

Thermocouple outputs were measured to 1 mV, which results in 0.1 °C sensitivity. A conservative estimate of the accuracy of the temperature measurement is ± 0.7 °C. The current input to the heater circuit was measured with a sensitivity of 0.01 A and accuracy of 0.6%. The power input to the circuit was then calculated by using the measured voltage drop across the circuit and its repective resistance. This procedure resulted in a maximum error of 3% in the calculated power inputs. The uncertainty associated with the length scale used in the data reduction is 1 mm. The thermophysical properties of air are assumed to be accurate within $\pm 3\%$ based on the observed variations in reported values in the literature.

The overall uncertainty in the Nusselt number varied with the power input and the bulk temperature of the coolant. The estimated uncertainties in the local Nusselt number are 2.64–4.44%. The maximum velocity measurement uncertainty is within $\pm 1\%$. In the calculation of friction factor and Reynolds number, the experimental uncertainties in friction factor and Reynolds number are 1.39–14.8% and 2.36–4.46%, respectively. These uncertainties represent the maximum deviation based on the absolute value of individual uncertainties. It should be noted that the uncertainty in these parameters is reduced when they are considered in terms of local values since the percentage error in the length measurement is decreased.

4. DATA REDUCTION

The local values of the thermophysical properties of air are obtained at a reference fluid temperature of

$$T_f = 0.5(T_{m1} + T_{m2}) \tag{1}$$

where T_{m1} and T_{m2} are the bulk temperatures of air at the inlet and outlet, respectively. The bulk temperature T_m is defined as

$$T_m = \left[\int_{r_i}^{r_o} T(r) W_m(r) r \, dr\right] \Big/ \left[\int_{r_i}^{r_o} W_m(r) r \, dr\right]. \tag{2}$$

The parameter D_h is defined as

$$D_h = 2(r_o - r_e) \tag{3}$$

which corresponds to a bare inner tube of radius r_e. A bare tube of radius r_e provides the same surface area as the finned tube, i.e.

$$r_e = r_i + [(e^2 + 2er_i) + (e + r_i)w]/p. \tag{4}$$

The local heat transfer coefficients used in the presentation of the data were calculated from

$$h_x = q''/(T_w - T_m) \quad (5)$$

where q'' is the heat flux of the inner test tube and $(T_w - T_m)$ is the temperature difference between the measuring point of the inner tube and the local air bulk temperature. The local Nusselt number is defined as

$$Nu_x = h_x D_h/k_f. \quad (6)$$

The complex flow field generated by the presence of the fins influences the pressure gradient required to drive the flow. A dimensionless measure of the pressure gradient is the Fanning friction factor, defined by

$$f_{app} = \Delta p^* D_h/x \quad (7)$$

where the differential pressure, Δp^*, has been nondimensionalized with respect to $\frac{1}{2}\rho W_m^2$ and W_m stands for local mean axial velocity.

5. RESULTS AND DISCUSSION

The present experimental study produces extensive information in terms of the flow, pressure and temperature field for flow past a fin element. Local heat transfer coefficients were also studied. Some important results are presented and discussed here.

5.1. *Flow visualization*

The present results focus mainly on the local steady state behavior. To view the local flow structure, a straw smoke generator was used under steady state conditions. The steady state condition was determined when the variation of temperature of the fin was less than 1% of that of its previous value. It usually takes 2 h to reach a steady state. It was found that the mean flow would suffer unsteadiness when $Re > 3000$. Typical flow patterns in the annular domain between the third and fourth fins are demonstrated in Figs. 4(a)–(d) for $w/e = 0.14$ and $p/e = 4$. Due to the experimental difficulty, this was only shown for $Re \leqslant 300$. Also shown in Fig. 4 is the major flow structure for the corresponding observation at each definite Reynolds number. At $Re = 100$, Fig. 4(a) basically shows a cell within two consecutive fins which indicates, due to a sudden change in the cross-section, that the flow separated at the tip of the fin. This causes the recirculating flow to occupy the entire region between two consecutive fins. However, the main flow moves downstream with a higher velocity, which results in nearly stagnant flow existing in the recirculating zone.

For a definite fin position, the location of the cell separation shear layer and the number of cells seem to be dependent on Reynolds number. As the Reynolds number increases, the location of the separation layer changes slightly, which can be seen in Figs. 4(b)–(d). This separation layer is located upstream near the corner of the fin, as shown in Figs. 4(a)–(c). However, in Fig. 4(d), it is found that this separation layer does not touch the fin wall and two cells exist in the recirculation zone. The fluid rises from the vertical face of the fin and flows over the upstream front face of the fin and the next fin. Inertia then carries the fluid across the cold surface of the main flow and then down the vertical wall opposite the fin. This phenomenon becomes more distinct as the Reynolds number increases until the cell may not have enough energy to maintain its recirculating motion. This is because the velocity of the main flow is so fast that the slow motion in the cell at low Reynolds number is unable to keep its original path, i.e. the cell is eventually broken into two cells at a Reynolds number of 300, as shown in Fig. 4(d). At low Reynolds numbers, the flow separates at the tip of the fin, but reattaches at the inner tube wall.

Figures 5(a)–(d) show the flow in the annular domain for $p/e = 6$ and 9 and two different Reynolds numbers, respectively. The common characteristics indicate that the dividing streamline at $p/e = 6$ is quite different from that of $p/e = 9$. The dividing streamline at $p/e = 6$ still occupied the entire region of the valley of the two consecutive fins. Similar situations occurred for $p/e = 4$, as shown in Figs. 4(a)–(d). However, at $p/e = 9$, the dividing streamline reattached to the plain wall in between two fins. Taking a closer examination of Figs. 4(a) and 5(a), it is found that the flow pattern was a little different. In Fig. 4(a) the dividing streamline never goes down toward the bottom as far as in Fig. 5(a). This is because an increase in p/e designates an increase in velocity in the transverse direction. This can also be seen in Figs. 5(b) and (c) for $p/e = 6$ and 9. In addition, an increase in Reynolds number designates an increase in velocity, which in turn increases the kinetic energy.

The effects of surface roughness width and concentrations of the surface roughness are shown in Figs. 6(a)–(d). Figure 6(a) illustrates that air flow passes over repeated fins with $p/e = 12$ and $w/e = 0.14$ at $Re = 100$. One can observe the presence of a medium recirculation zone in a cycle compared with those of $p/e = 4$ and 6 for $w/e = 0.14$ at the same Reynolds number. The dividing streamline, separating the main flow and recirculating region, never touches the inner wall of the tube. Comparison of Figs. 6(a) and (b) shows that the streamwise length of the recirculation zone appears to increase with Re. Again, this indicates that the Reynolds number increase designates an increase in the velocity. As a consequence, the dividing streamline in Fig. 6(b) can move slightly further down to the wall. On the other hand, due to the difference of the width ($w/e = 0.83$) of the surface roughness in Figs. 6(c) and (d), a different phenomenon was observed. Unfortunately, experimental data for higher w/e seem to be lacking. Only $w/e = 0.83$ was studied. However, at this stage, one may conclude that the flow seems much more disturbed for higher w/e because additional recirculation zones may occur [15].

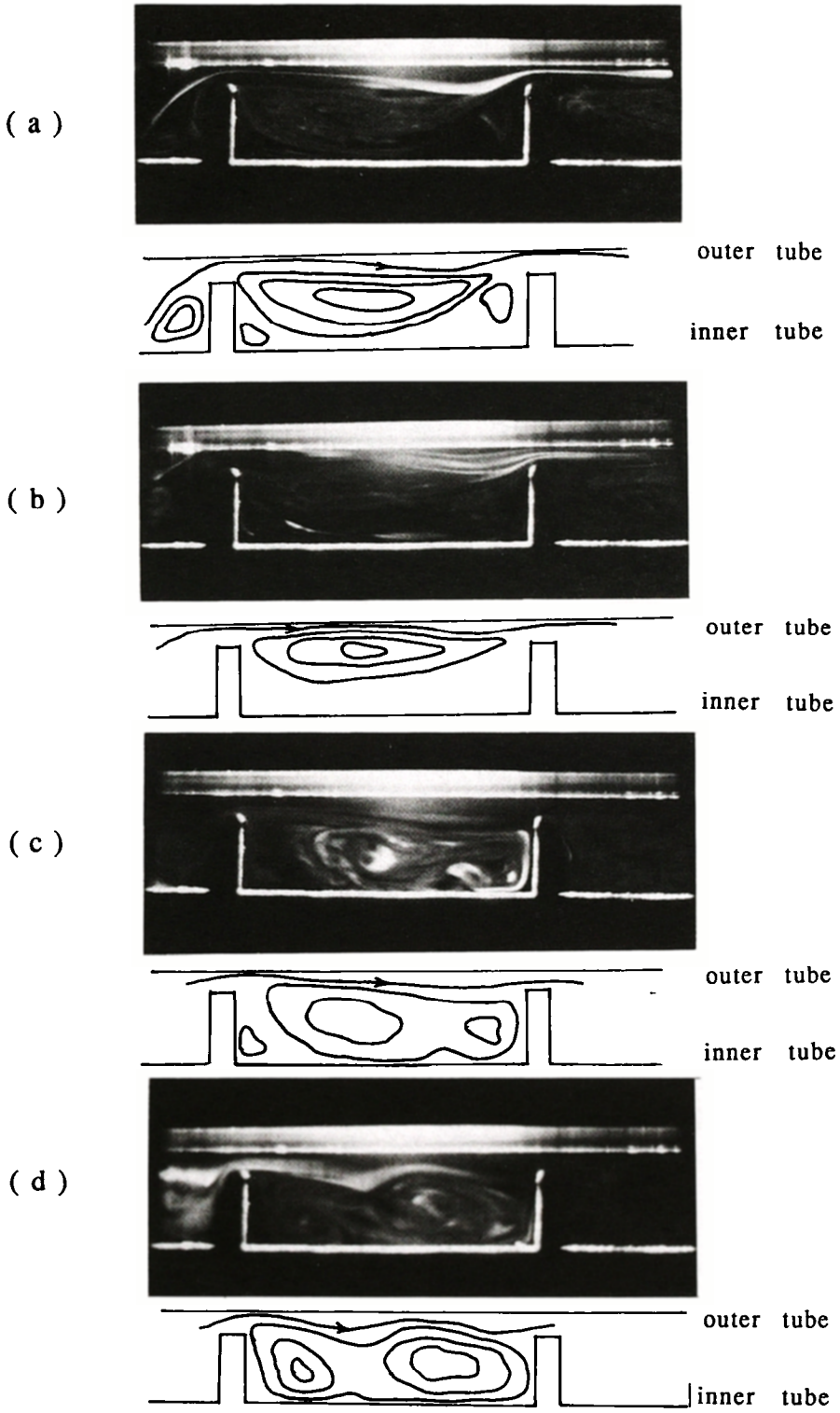

FIG. 4. Photographs made by flow visualization for $w/e = 0.14$: (a) $Re = 100$, $p/e = 4$; (b) $Re = 200$, $p/e = 4$; (c) $Re = 250$, $p/e = 4$; (d) $Re = 300$, $p/e = 4$.

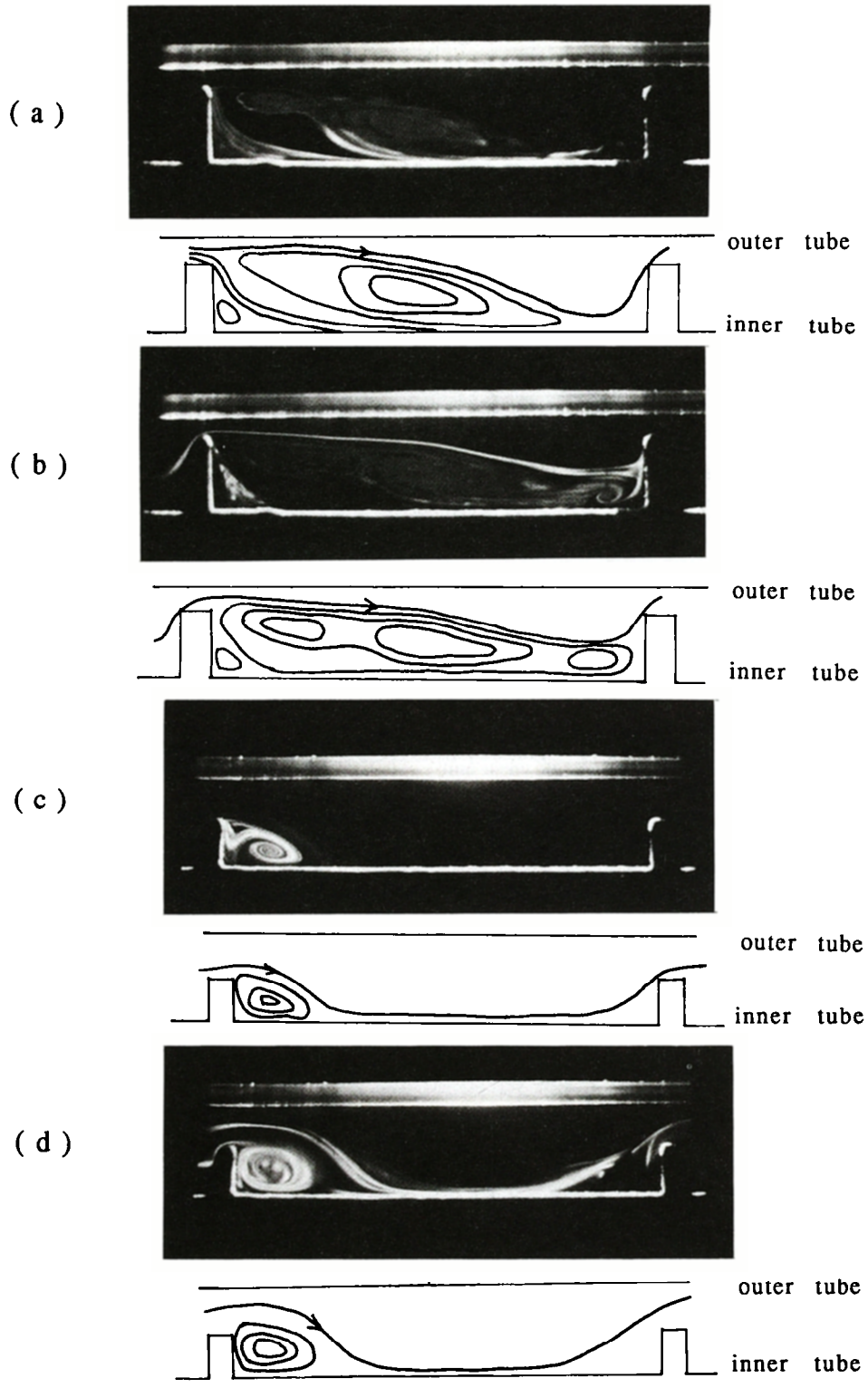

FIG. 5. Photographs made by flow visualization for $w/e = 0.14$: (a) $Re = 100$, $p/e = 6$; (b) $Re = 200$, $p/e = 6$; (c) $Re = 100$, $p/e = 9$; (d) $Re = 200$, $p/e = 9$.

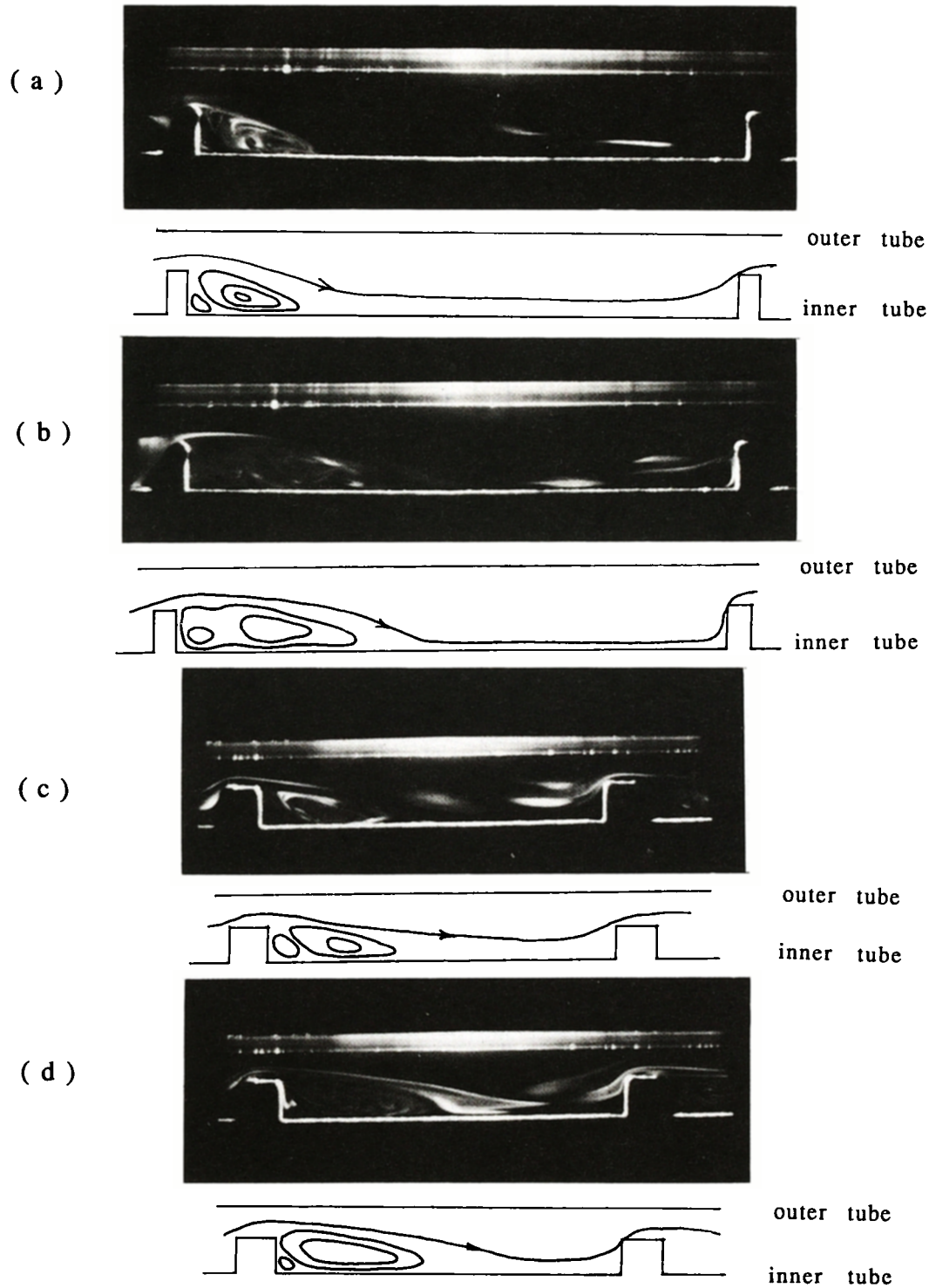

FIG. 6. Photographs made by flow visualization: (a) $Re = 100$, $p/e = 12$, $w/e = 0.14$; (b) $Re = 200$, $p/e = 12$, $w/e = 14$; (c) $Re = 100$, $p/e = 9$, $w/e = 0.83$; (d) $Re = 200$, $p/e = 9$, $w/e = 0.83$.

5.2. *Local friction factor*

The pressure distributions in between two consecutive fins (the third and fourth fins in the present study) in a finned annulus ($p/e = 6$) at Reynolds numbers of 1000, 1500 and 3000 are shown in Fig. 7. There is a high pressure gradient near the fin and in between the two consecutive fins. However, a small pressure recovery is observed in the reattachment region. The pressure drop was measured successively from inlet to outlet of the test tube for laminar flow. Reynolds numbers based on the hydraulic diameter D_h ranged from 1000 to 3000. Further examination of Fig. 7

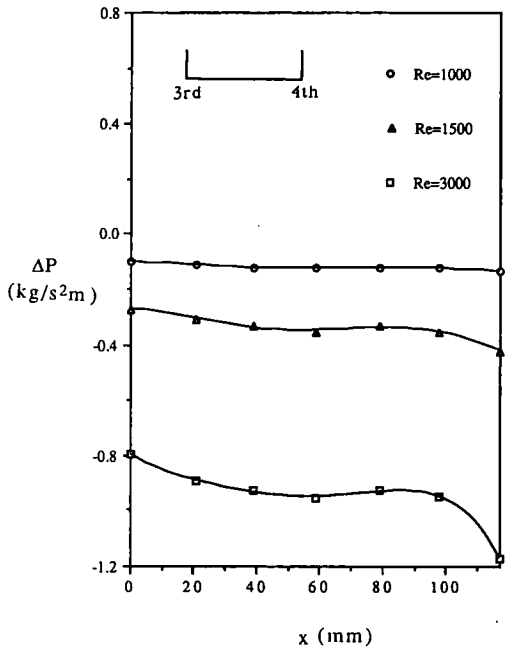

FIG. 7. Pressure drop (between the third and fourth fins) along the outer wall, $p/e = 6$.

shows that the pressure gradient at the point right before or after the fin was much larger. This is because at the corners of these points, shedding vortices cause large pressure drops. This situation is quite similar to that expected from Sinha *et al.* [16]. Moreover, from Fig. 7, the pressure distribution has two inflection positions due to flow reattachment and separation. Each of these inflection points corresponds to a separation or reattachment point, respectively. One thing we need to address here is that the reattachment and separation points would be slightly delayed as the Reynolds number increases. This is also shown by the previous findings with flow visualization in the preceding section. The pressure drop becomes large as the Reynolds number increases. This is because the Reynolds number increase designates an increase in the velocity, which in turn causes a larger rate of change of momentum resulting in a larger pressure drop.

A dimensionless measurement of the pressure gradient is the friction factor defined by equation (7). Figure 8(a) presents the variation of friction factor with different p/e at a definite Reynolds number of 1000. Owing to an extreme velocity change near the inlet of the annuli causing a high momentum change, the distribution generally shows a monotonic decrease for the friction factor as the downstream distance increases. The friction factor for the smooth annulus maintains the lowest value, as one would expect. In addition, it is found that the local friction factors varied from low values at low p/e to a maximum value near $p/e = 6$ and then decreased at high p/e. It is interesting to note that the local friction factor inverses slowly with p/e when it is less than 6, while, for values of p/e greater than 6, the local friction factor falls quite dramatically. The reason for this may be explained in the way that for small fin pitch-to-height ratio, for instance $p/e = 4$, the flow which separates after each fin does not reattach before it reaches the succeeding fin. The local friction factor increased with p/e values greater than 4 because of the increase in the form drag from each fin element. At a p/e value of about 6, the flow nearly reattached to the succeeding fin. For larger fin spacing, the reattachment point is reached and a boundary layer starts to grow before the succeeding fin is encountered. This reduces the average shear stress. In general, a higher value of friction factor represented a large penalty, which was increased when the finned tube was considered. Figure 8(b) shows the friction factor distribution along the downstream distance for different Reynolds numbers at $p/e = 6$. The accuracy of the local friction factor measurement was about $\pm 2.3\%$, which is reflected in the size of the data points. In this figure, the distribution exhibits a definite trend, as in Fig. 8(a), and this distribution approaches an asymptote as x^+ increases further to a certain value (say, $x^+ = 0.20$, present study). At a definite downstream station, f_{app} decreases as the Reynolds number increases. This is due to a smaller boundary layer thickness at higher Reynolds number and, consequently, it reduces the skin friction. Finally, a plot of $f_{app}\,Re$ against x^+ ($x^+ = 0$ corresponding to the inlet of the test section), along with a smooth annulus result reported by Liu [17], is shown in Fig. 9. The agreement with the present smooth data is extremely good. The $f_{app}\,Re$ of each annulus is correlated in terms of $x/(D_h\,Re)$ in the form:

$$f_{app}\,Re = C\left(\frac{x}{D_h\,Re}\right)^m. \tag{8}$$

Constant C, exponent m and standard deviation σ_1 are given in Table 2. These correlations represent the raw numerical data with a maximum error of 9.8%.

5.3. *Temperature distribution*

Figure 10 shows the streamwise distribution of dimensionless wall temperature for different finned tube annuli with smooth data considered as a reference. As one would expect, for the longitudinally/peripherally constant heat flux of the present study, the thermally fully developed region is characterized by wall and bulk mean temperatures. Both increases are almost a linear function of downstream distance. After the flow reaches a certain downstream distance, it is found that flow would become fully-developed because the slope of the curve approaches a near zero value. This also means that the temperature difference between the wall temperature and that of the bulk mean remains unchanged. In addition, the dimensionless wall temperature of $p/e = 12$ is the lowest among these curved all the way down to the downstream end. However, the smooth data exhibit a middle value. This indicates

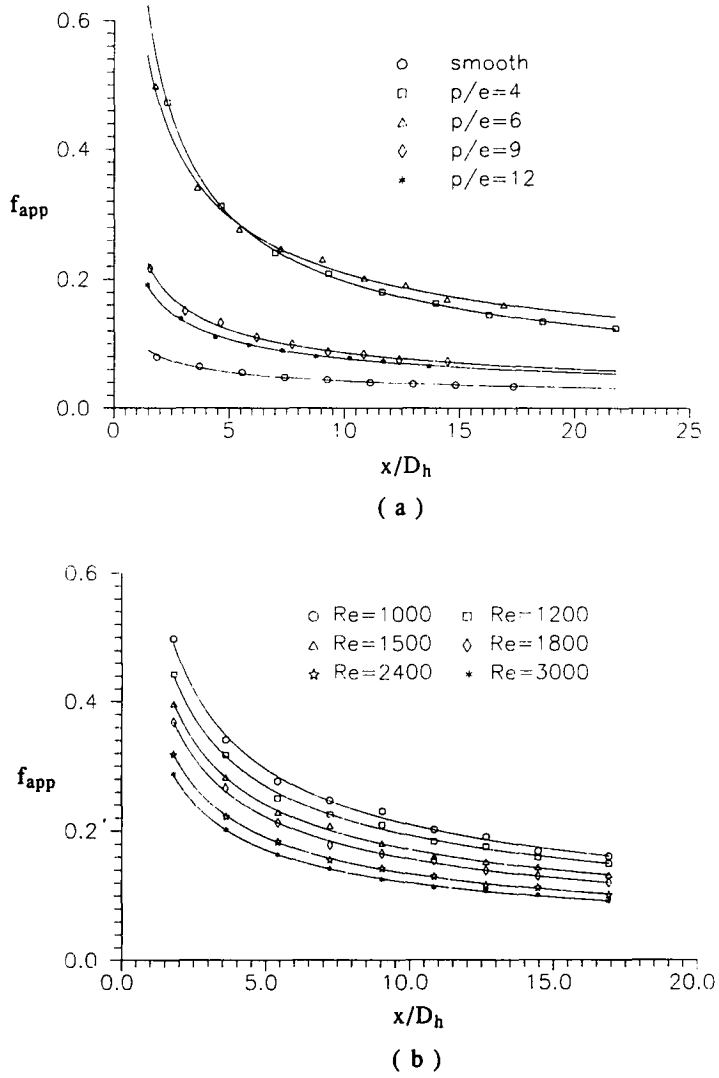

FIG. 8(a). Friction factor distribution with different p/e values along the downstream distance, starting from the inlet of test section; $Re = 1000$. (b). Friction factor distribution with different Re along the downstream distance, starting from the inlet of test section; $p/e = 6$.

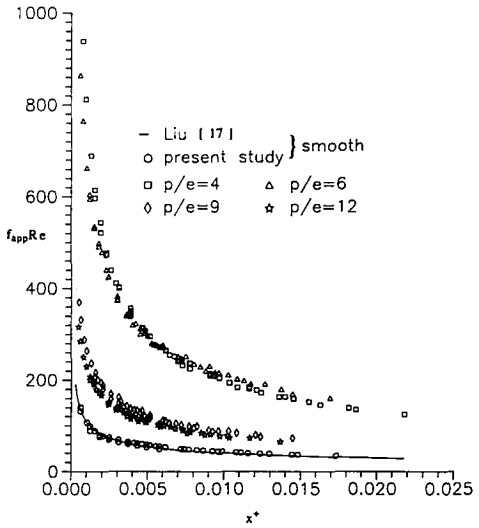

FIG. 9. Plot of $f_{app}\,Re$ vs x^+ with different p/e.

that the finned tube annulus of $p/e = 4$ was no good as far as heat transfer enhancement is concerned. This can also be clearly noted in a later section. Further inspection of the temperature distribution shows that finned tube annuli of $p/e = 6$ and 9 seem to have the

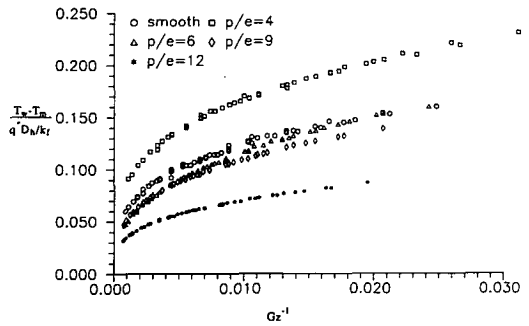

FIG. 10. Variation of dimensionless temperature difference against Gz^{-1} with different p/e.

Table 2. Coefficients C and C_1, exponents m and n, and deviations σ_1 and σ_2 for friction factor and Nusselt number correlations (equations (8) and (9))

Annulus	C	C_1	m	n	σ_1	σ_2
Smooth	6.92	2.99	−0.39	0.25	0.378	0.549
$p/e = 4$	12.34	1.66	−0.60	0.28	0.677	0.074
$p/e = 6$	21.11	1.55	−0.49	0.38	1.080	0.501
$p/e = 9$	9.24	2.13	−0.48	0.32	0.108	0.280
$p/e = 12$	9.18	3.65	−0.46	0.30	0.505	0.414

same influence on heat transfer rate. To gather further understanding of the thermal field of this study, Figs. 11(a)–(d) show interferograms of the temperature field in finned tube annulii within two consecutive fins (the third and fourth fins for the present study) in the infinite fringe mode for $p/e = 9$ and 12 with two different Reynolds numbers of 500 and 1000, respectively. The resulting figures are isotherms.

Close-up views of the air channel flow at $Re = 500$ and 1000 for $p/e = 9$ and 12 are shown in the interferograms in Fig. 11. The measured isotherm patterns in Fig. 11 indicate that the surface heat flow is reduced along the wall just before and after the fin element compared with what it would be on a smooth annulus. The temperature gradient at the front surface of the fin appears to be high, especially near the lower front surface of the fin. This characteristic is similar to that reported by Aung [18], investigating laminar forced convection downstream of backsteps. Furthermore, at $Re = 500$, the present isotherm patterns in Fig. 11(a) along the tube wall coincided with the previous findings of the flow patterns because they show that the thermal boundary layers interact with the flow. The fringe closest to the wall is so thick that the heat transfer rate is low as it approaches the tube walls. The higher order fringes possess higher cur-

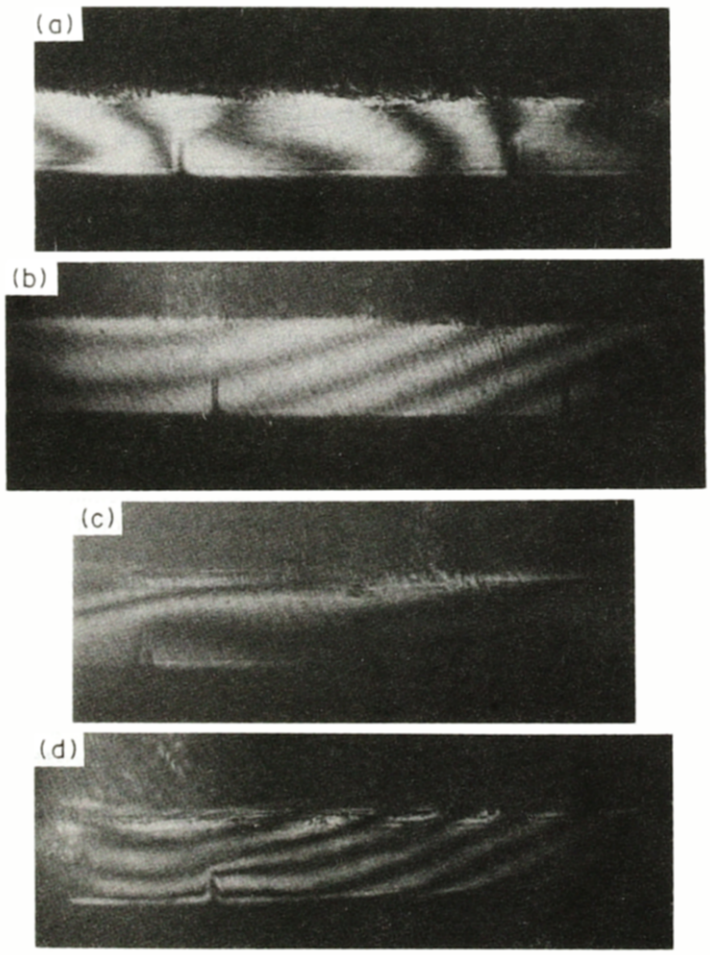

FIG. 11. Photographs made by thermal field visualization: (a) $Re = 500$, $p/e = 9$; (b) $Re = 1000$, $p/e = 9$; (c) $Re = 500$, $p/e = 12$; (d) $Re = 1000$, $p/e = 12$.

vature due to separation/recirculation. This also explains why at the upstream end of the inter-fin space (close to the left fin), spacing between isotherms is large, indicating a region of low temperature gradient for $p/e = 9$ at $Re = 500$. This condition is caused by a stagnant flow in the region, which restricts heat transfer to diffusion only. At the downstream end, however, close to the right fin, the isotherms are closely spaced. When Re becomes higher ($= 1000$), shown in Fig. 11(b), previous isotherms change slightly. The thermal boundary layer seems to become thinner and, consequently, results in a higher heat transfer. These two distinct characteristics can be explained in the way that, at $Re = 1000$, the fringes are thinner compared to those at $Re = 500$. At $Re = 500$, due to the recirculation-like flow in between two consecutive fins, arc-shaped isotherms occur everywhere near the vicinity of the fin. The fringe was thickened the most. This also verified the previous findings based on the flow visualization. On the contrary, for $p/e = 12$ shown in Figs. 11(c) and (d), the isotherm pattern shows a completely different trend, especially at $Re = 500$ (Fig. 11(c)). The fringe in the entire flow never seems to touch the side wall except near the rear part of the fin, where an extremely thickened fringe exists. This also indicates that there exists a shedding vortex right after the flow passes over the fin, when $p/e = 12$ at $Re = 500$. As Re is increased to 1000, in Fig. 11(d), the fringe is thinned the most and the width of the fringe has changed along its path when compared to the corresponding isotherms for $p/e = 9$ shown in Fig. 11(b). When fringes become thinner and get close to each other, this implies a region of higher heat transfer which can be seen from Fig. 11(b) for the flow passing over the fin and along the tube wall. In summary, closely spaced fins (small p/e) actually decrease heat transfer. Thus, the heat transfer rate would improve if the fins were further apart (say, $p/e = 12$ for the present study).

5.4. *Local Nusselt number distribution*

As stated earlier in the Experimental Apparatus section, the present experimental set-up is capable of obtaining local heat transfer results at any point on the surface of interest. To ease data interpretation for this study, the local results are presented as spanwise average along the downstream direction perpendicular to the fins. Figures 12 and 13 show plots of the spanwise-averaged Nusselt number, Nu_x, at different p/e and Reynolds number. Figure 13 also presents the entrance effect on the local Nusselt number distribution.

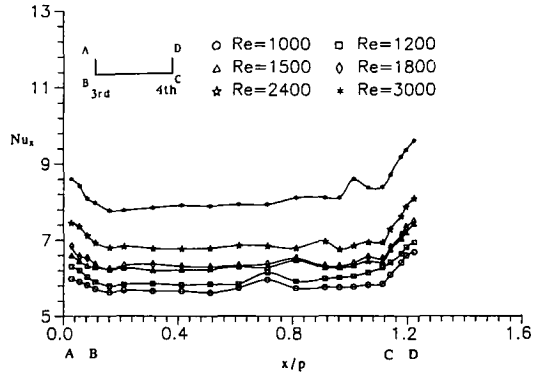

FIG. 12. Local Nusselt number (between the third and fourth fins) distribution with different Reynolds numbers at $p/e = 9$.

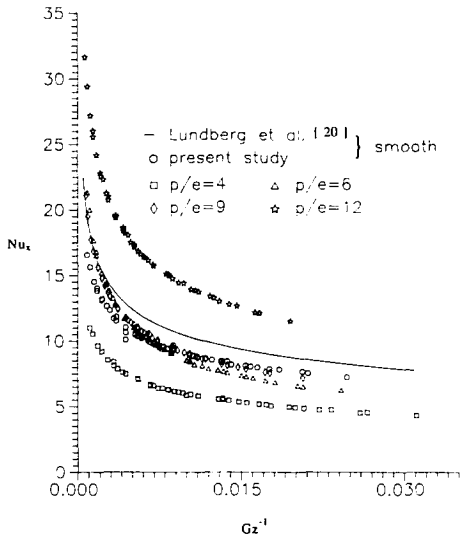

FIG. 13. Plot of Nu_x vs Gz^{-1} with different p/e.

In Fig. 12, the values of Nu_x along the floor surface between the third (left) and fourth (right) fins are plotted against downstream distance. In general, the fin tip and sides display the presence of significantly higher convection rates than the floor between fins for all the Reynolds numbers investigated. This further indicates that from the left (upstream) fin, heat transfer is higher at the tip and decreases to a certain lower value at the floor. Heat flux from the inner tube increases in the downstream direction until a peak value, which occurs near the center of the recirculation eddy, is reached. Thereafter the heat flux decreases until the floor of the right (downstream) fin is reached, where it is zero. Heat transfer in the downstream region is high due to increased convection aided by higher velocities in the recirculation eddy. This effect becomes more pronounced as the Reynolds number is increased further. Maximum heat transfer occurs at the tip of the right (downstream) fin, where the main flow reattaches. These effects were also observed by Agrawal and Sengupta [13]. It can also be inferred from Fig. 12 that heat transfer from the downstream end of the fin is several times (1.05–1.2) higher than that from the upstream end. This may be caused by the separated shear layer either reattaching on the forward facing side of the downstream fin or skimming over the cavity. As a result, the near wall region between two adjacent fins is filled with a recirculating bubble. The local maximum of Nu_x, lying just ahead

of the downstream fin, may be attributed to the unsteadiness of flow in the region, as repored earlier by William and Watts [19]. In their study, a periodic flow behavior with intermittent vortex shedding near a fin front corner was observed, and this effect enhances the heat exchange between the corner region and the core flow. Maximum heat transfer occurs at the tip of the right (downstream) fin where the main flow reattaches.

Figure 13 strongly suggests that the present study is in the thermally developing region until Gz^{-1} reaches 0.030, which was shown in the preceding section for the friction factor. Based on Fig. 13, Nu_x monotonically decreases as Gz^{-1} increases, as does the local friction factor. This would not exhibit some sort of cyclic nature as mentioned earlier. This is because the calculations of friction factors and Nusselt numbers were based on the averaged pressure drops and temperature differences. The heat transfer rates with finned tube data of the annuli are obtained and presented for $p/e = 4$, 6, 9 and 12. The data of the present bare tube annulus were compared with those of Lundberg *et al.* [20] investigating the thermal entry length problem for a concentric annular duct, with a good agreement for tendency and magnitude. The deviation was mainly caused by different geometries and boundary conditions. Finally, the local Nu_x of each finned annulus, including bare tube, with the conventional parameter Gz (Graetz number) is further correlated in the form:

$$Nu_x = C_1(Gz)^n. \tag{9}$$

Constant C_1, exponent n and standard derivation σ_2, are also given in Table 2. These correlations represent the raw numerical data with a maximum error of 13.03%.

6. CONCLUSION

An experimental study was conducted for laminar entrance flow and heat transfer in finned tube annuli. The nature of flow and heat transfer in finned tube annuli was investigated in the range of $100 \leqslant Re \leqslant 3000$, $4 \leqslant p/e \leqslant 12$ and two width-to-height ratios to broaden our basic understanding of this type of convective heat transfer. Flow and thermal field visualizations were made to give additional insight into the physical phenomena. The most significant contributions of the present study are the following.

(1) Flow visualization indicates that the existence of protruding fins changes the flow characteristics and originates the separation/recirculation zone as well as the local turbulent zone in the vicinity of the fins.

(2) The presence of protruding fins results in the formation of separation/recirculation zones in the flow field, yielding a substantially higher friction factor. The local friction factor increases with p/e to a maximum value near $p/e = 6$ and then decreases at high p/e.

(3) The friction factor data (using pitot tube and pressure transducer), the heat transfer data (using laser holographic interferomery and thermocouple temperature measurement) and flow visualization strongly suggest that the flow separation/recirculation and entrance effects are the two major factors influencing the pressure drop and the temperature in finned tube annuli.

(4) It is found, only for $p/e = 12$, that the local Nusselt number at the downstream end of finned tube annuli is about 1.2 times higher than that of a smooth annulus. The reason for this was discussed in detail.

(5) Systematic experimental data for the local friction and local Nusselt number in the geometric configuration described were obtained and relevant correlations were established.

Acknowledgement—This work was supported by a research grant (NSC80-0401-E110-12) from the National Science Council, Taiwan, Republic of China.

REFERENCES

1. R. L. Webb, E. R. G. Eckert and R. J. Goldstein, Heat transfer and friction tube with repeated-rib roughness, *Int. J. Heat Mass Transfer* **14,** 601–617 (1971).
2. R. L. Webb and E. R. G. Eckert, Application of roughness surface to heat exchanger design, *Int. J. Heat Mass Transfer* **15,** 1647–1658 (1972).
3. J. C. Han, L. R. Glickman and W. M. Rohsenow, An investigation of heat transfer and friction for rib-roughed surfaces, *Int. J. Heat Mass Transfer* **21,** 1143–1156 (1978).
4. S. W. Hang and A. E. Bergles, Augmentation of laminar flow heat transfer by means of twisted tape inserts, *ASME J. Heat Transfer* **98,** 251–256 (1978).
5. W. J. Marner and A. E. Bergles, Augmentation of tube side laminar flow heat transfer by means of twisted tape inserts and internally finned tubes, *Proc. Sixth Int. Heat Transfer Conf.* (Toronto), Vol. 2, pp. 583–588 (1978).
6. R. S. Van Rooyen and D. G. Kroger, Laminar flow heat transfer augmentation in internally finned tubes with twisted tape inserts, *Proc. Sixth Int. Heat Transfer Conf.* (Toronto), Vol. 2, pp. 578–581 (1978).
7. A. E. Bergles and S. D. Joshi, Augmentation techniques for low *Re* in tube flow. In *Low-Reynolds Number Flow Heat Transfer Exchanger* (Edited by S. Kakac, R. K. Shah and A. E. Bergles), pp. 694–720. Hemisphere, Washington, DC (1983).
8. J. E. O'Brien and E. M. Sparrow, Corrugated-duct heat transfer pressure drop, and flow visualization, *ASME J. Heat Transfer* **104,** 410–416 (1982).
9. B. W. Webb and S. Ramadhyani, Conjugate heat transfer in a channel with staggered ribs, *Int. J. Heat Mass Transfer* **28,** 1679–1687 (1985).
10. K. M. Kelkar and S. V. Patankar, Numerical prediction of flow and heat transfer in a parallel plate channel with staggered fins, *ASME J. Heat Transfer* **109,** 25–30 (1987).
11. G. J. Rowley and S. V. Patankar, Analysis of laminar flow and heat transfer in tubes with internal circumferential fins, *Int. J. Heat Mass Transfer* **27,** 553–560 (1984).
12. A. T. Prata and E. M. Sparrow, Heat transfer and fluid flow characteristic for an annulus of periodically varying cross-section, *Numer. Heat Transfer* **7,** 285–304 (1984).
13. A. K. Agrawal and S. Sengupta, Laminar flow and heat

transfer in a finned tube annulus, *Int. J. Heat Fluid Flow* **11,** 54–59 (1990).
14. W. Aung and R. O'Regan, Precise measurement of heat transfer using holographic interferometry, *Rev. Scient. Instrum.* **42,** 1755–1758 (1971).
15. Y.-J. Hong, S.-S. Hsieh and H.-J. Shih, Numerical computation of laminar separation and reattachment of flow over surface mounted ribs, *ASME J. Fluids Engng* **113,** 290–198 (1991).
16. S. N. Sinha, A. K. Gupta and M. M. Oberai, Laminar separation flow over backsteps and cavity, part 2 : cavity, *AIAA J.* **20,** 774–781 (1982).
17. J. Liu, Flow of a Bingham fluid in the entrance region of an annular tube, M.S. Thesis, University of Wisconsin-Milwaukee (1974).
18. W. Aung, An experimental study of laminar heat transfer downstream of backsteps, *ASME J. Heat Transfer* **105,** 823–829 (1983).
19. F. William and J. Watts, The development of rough surface with improved heat transfer performance and a study of the mechanisms involved, *4th Int. Nat. Heat Transfer Conf.* (Versailles), FC5, p. 4 (1970).
20. R. E. Lundberg, W. C. Reynolds and W. M. Kays, Heat transfer with laminar flow in concentric annuli with constant and variable wall temperature and heat flux, NASA Tech. Note TN-1972 (1963).